Article:
Taylor, CM, Belušić, D, Guichard, F et al. (7 more authors) (2017) Frequency of extreme Sahelian storms tripled since 1982 in satellite observations. Nature, 544 (7651). pp. 475-478. ISSN 0028-0836

https://doi.org/10.1038/nature22069

A three-fold rise in frequency of extreme Sahelian storms observed since 1982

Christopher M. Taylor[1,2], Danijel Belušić[1,3], Françoise Guichard[4], Douglas J. Parker[5], Théo Vischel[6], Olivier Bock[7], Philip P. Harris[1,2], Serge Janicot[8], Cornelia Klein[1], Gérémy Panthou[6]

[1] Centre for Ecology and Hydrology, Wallingford, OX10 8BB, U.K.

[2] National Centre for Earth Observation, Wallingford, U.K.

[3] Swedish Meteorological and Hydrological Institute, Norrköping, Sweden

[4] CNRM, UMR 3589, CNRS & Météo-France, Toulouse, France

[5] School of Earth and Environment, University of Leeds, Leeds, LS2 9JT, UK

[6] Univ. Grenoble Alpes, Grenoble INP, IGE, F-38000 Grenoble, France

[7] IGN LAREG, Univ. Paris Diderot, Sorbonne Paris Cité, Paris, France

[8] UMR7159 LOCEAN, Sorbonne Universités UPMC-CNRS-IRD-MNHN, Paris, France

Accepted for publication in Nature – NOT FOR DISTRIBUTION

The hydrological cycle is expected to intensify under global warming[1], with studies reporting more frequent extreme rain events in many regions of the world[2-4], accompanied by expected increases in future flood frequency[5]. These early, predominantly mid-latitude observations are critical because of short-comings within climate models in their depiction of convective rainfall[6,7]. A globally important group of intense storms, Mesoscale Convective Systems (MCSs[8]), pose a particular challenge as they organise dynamically on spatial scales which cannot be resolved by conventional climate models. Here we use 35 years of satellite observations from the West African Sahel to reveal a persistent increase in the frequency of the most intense MCSs. Sahelian storms are some of the most powerful on the planet[9], and gauges here have recorded a rise in extreme daily rainfall totals. Intense MCS frequency is only weakly related to the multi-decadal recovery of Sahel annual rainfall, but is highly correlated with global land temperatures. Analysis of trends across Africa reveal that MCS intensification is limited to a narrow band south of the Sahara desert. During this period, wet season Sahelian temperatures have not risen, ruling out rainfall intensification in response to locally warmer conditions. On the other hand, the meridional temperature gradient spanning the Sahel has increased in recent decades, consistent with anthropogenic forcing driving enhanced Saharan warming[10]. We argue that Saharan warming

intensifies convection within Sahelian MCSs through increased wind shear, and changes to the Saharan Air Layer (SAL). The meridional gradient is projected to strengthen throughout the 21st century, suggesting the Sahel will experience particularly marked increases in extreme rain. The remarkably rapid intensification of Sahelian MCSs since the 1980s sheds new light on the response of organised tropical convection to global warming, and challenges conventional GCM projections.

The Clausius-Clapeyron relationship indicates that the water holding capacity of the atmosphere increases by ~6-7% per 1°C. Assuming that humidity is the main driver of extreme rain, and that relative humidity remains constant, changes in extreme rainfall scale with temperature according to this relationship[7]. The scaling is largely reproduced by GCMs in the extra-tropics, but is highly variable across models in the tropics[11]. Rising temperatures may also intensify storm-scale dynamics, enhancing moisture inflow and the overall precipitation efficiency of rain events[12,13], features which are not well-captured by GCMs; the importance of these processes for extreme rainfall likely depends on details of the local environment[14]. The difficulty in simulating these processes at multiple scales, coupled with a general lack of long-term tropical observations, makes uncertainty in future projections of extreme tropical rainfall particularly high[7]. These gaps in fundamental knowledge of the climate system are of major societal importance for the populations who live in tropical land regions, not least Africa, where the vast majority of agriculture is rain-fed, and resilience of infrastructure to climatic change is low.

We focus on data from the modern satellite era (1982-2016) across the Sahel, the semi-arid region to the south of the Sahara. Sahel rainfall occurs during the active West African Monsoon (WAM) months of June-September (JJAS), with approximately 90% of rain due to MCSs[15]. These travelling systems can extend many 100s kms, with lifetimes which may exceed 1 day[16], but locally, rain typically falls within a couple of hours associated with a line of convective cells at the front of the MCS. The Sahel experienced extreme decadal variability in rainfall during the 20th century, with profound drought during the 1970s and 1980s following a very wet period in the 1950s and 1960s[17] (Extended Figure 1). Since the late 1990s, the 5-year mean rainfall has recovered to more stable intermediate levels but retained strong interannual variability. Many researchers have emphasised the role of oceanic forcing on the decadal variability[18] whilst recent studies have argued that the recovery is primarily driven by anthropogenic emissions of greenhouse gases[19]. At the same time, daily gauge totals[17] (Figure 1b) illustrate a marked rise in extreme rainfall (see Methods), above and beyond that observed during the very wet decades preceding the drought, and continuing to rise since the so-called recovery.

We characterise properties of MCSs using cloud-top temperature from thermal infra-red sensors onboard the geostationary Meteosat series. Whilst cloud-top temperature does not directly relate to rainfall, it is well-suited to documenting the life cycle of MCSs[15,16], and moreover, Meteosat provides a unique sub-daily time series of storms over more than 3 decades. For every Meteosat image, we define an MCS as a contiguous cold cloud system exceeding 25,000 km^2. More than 85% of extreme daily raingauge totals coincide with the passage of an MCS using the widely-used threshold for cold cloud of -40°C (Methods). However, the likelihood of extreme rain increases strongly with decreasing cloud-top temperature, as shown from both daily gauge accumulations, and instantaneous spaceborne radar estimates (Extended Figure 2). Colder (hereafter, more "intense") MCSs are also associated with increases in both the fractional area of convective rain and westward propagation speed (see Methods).

The time series of MCS frequency at -40°C is highly correlated with seasonal mean rainfall (Table 1), consistent with previous studies[15]. In Figure 1 c and d we show trends in MCS frequency sampled at 1800 UTC, a time when typically, MCSs have reached their mature phase[16]. Interestingly, as the temperature threshold is reduced, the time series start to resemble strong linear trends. At a threshold of -70°C, the trend at 1800 UTC amounts to a remarkable 3.5 fold increase over 35 years, or 3.7 when averaged over 24 hours (Extended Figure 3). The rise in intense MCS frequency is driven by a downward trend in MCS mean temperature (0.78°C per decade for -40°C systems; Extended Figure 4). Intense MCS frequency is highly correlated with global land temperature (Table 1), yielding sensitivities of +99% (-70°C) and +200 % (-75°C) per degree of global land temperature. Importantly, the rise in frequency of intense MCSs has continued since the so-called recovery of the late 1990s, in the absence of a trend in annual rainfall i.e. the intensification signal emerges above the strong decadal variability of total rainfall in this region[17].

The spatial extent of the trend in intense African MCSs is restricted in JJAS to a narrow Sahelian belt Figure 1e). Trends over the full annual cycle (Extended Figure 5) show the signal extends down to the Guinea Coast during boreal spring, but there is no evidence of similarly extensive trends elsewhere in Africa, including the Congo Basin, another global hotspot of intense storms[9]. Analysis of the diurnal cycle (Extended Figure 3) indicates that positive trends in MCS frequency at -70°C are significant ($P<0.005$) at all times of day, and are in phase with the typical MCS life cycle of afternoon initiation, peak frequency in the evening, and decay during the morning hours. Positive trends in the size of the largest MCSs are modest for most times of day and temperature thresholds, and become significant ($P<0.01$) during the evening for the most intense systems. At all times of day however, the trend in total coverage of the coldest systems is dominated by changes in frequency, not area. The diurnal

phase of these trends implies that they are driven by more intense convection in late afternoon and evening, in turn creating larger, longer-lived systems overnight.

Potential drivers of this rapid regional intensification of MCSs include mineral aerosol concentrations and vegetation cover, though neither exhibit a well-defined trend including the last 10 years[20,21]. Instead, the high correlation with global temperature suggests a response to atmospheric warming. Observational and reanalysis datasets agree that near-surface Sahelian temperature trends (JJAS) over this period have been small or negative (Figure 2), presumably a direct response to increased rainfall, cloud, and surface evaporative cooling following the multi-decadal drought. The intensification of MCSs cannot therefore be a simple response to rising local temperature. However there is a consensus across datasets that the Sahara has been warming more rapidly than the rest of Africa[19,22], though spatial patterns differ, linked to the sparse and temporally varying measurement network. Saharan warming has therefore driven an increase in the meridional temperature gradient. Whilst most historical CMIP5 GCM simulations do not capture the Sahelian drought recovery, the trend in simulated temperature gradient is a robust response across the ensemble to greenhouse gas emissions, and is projected to continue to intensify throughout the 21st century (Figure 2e).

We now consider the role of atmospheric variables known to influence MCS properties, through correlations with MCS intensity at both event (Extended Figure 7) and annual (Extended Figure 8) time scales (see Methods). Firstly, it has been known for several decades that wind shear organises convection into long-lived and large-scale systems[23]. We find significant correlations ($P<0.005$) between pre-MCS zonal wind shear and MCS intensity, consistent with recent theory that shear dominates the intensity of MCSs[24]. The intensification trend is also correlated with increasing low-level westerlies, and the African Easterly Jet. Secondly, mid-level dry air intensifies Sahelian MCSs (via enhanced evaporative downdraughts)[25,26] and we find significant correlations with 700 hPa relative humidity on both time scales. Another important factor for convection is low level moisture; a dry Planetary Boundary Layer (PBL) tends to suppress the development of MCSs through lack of Convective Available Potential Energy (CAPE). Interestingly, we find no significant correlation with low level specific humidity at either the event or annual time scales, a factor we return to below. We do however find event-scale relationships between MCS intensity and both higher temperatures, and weaker southerly winds at low and mid-levels. These variables are not independent, and in particular, co-vary with the phase of African Easterly Waves (AEWs), the dominant synoptic feature in the region. With the exception of mid-level temperature however, their respective correlations at event and annual scales differ in sign (see Methods), suggesting trends in these variables cannot explain intensification. Mid-level warming suppresses the early development of small convective clouds, therefore allowing the accumulation of more CAPE, and more intense systems to develop

once they have been triggered. Considering synoptic variability, AEWs modulate MCS frequency, and climate projections indicate more intense AEWs by 2100 under greenhouse forcing[27], driven by increasing baroclinicity. Whilst we are unaware of previous work showing observed multi-decadal trends in AEWs, we note the strong correlation (Extended Figure 8f) between MCS intensity and enhanced low level synoptic variability to the north of the Sahel in ERA-Interim, suggestive of a role in MCS intensification. Finally, widespread tropopause cooling has been reported as a response to greenhouse gas emissions. Because upper tropospheric observations and reanalyses are unreliable in this data sparse region[28], one cannot rule out a role for this process in MCS intensification.

The observed increase in extreme precipitation inferred from MCS properties has not been accompanied by trends in precipitable water (PW) or specific humidity (Extended Figure 8). Composite time series of PW measurements (Methods) depict a rapid moistening in the 3-4 hours ahead of an MCS (Figure 3) due to moisture flux convergence. Whilst MCS intensity is highly correlated with PW at the time of passage, there is no significant signal with PW when measured 6 hours ahead. This is an example of MCS-scale dynamic processes leading to rainfall intensification beyond the limits of the local thermodynamic profile - the same dynamic processes can explain our observed multi-decadal trends. We conclude that the most likely drivers of Sahelian MCS intensification are enhanced shear, and drying at mid-levels, consistent with well-established mechanisms. In addition, mid-level warming and enhanced synoptic variability could have played a role. These mechanisms are all directly linked to a warming Sahara; baroclinicity enhances shear and drives AEWs, whilst the mid-level SAL in the Sahel is adiabatically connected to the Saharan PBL[29].

Assuming the current physical relationships linking Saharan warming with Sahelian MCS intensity still hold, projections of enhanced baroclinicity imply that extreme daily rainfall totals will continue to rise rapidly, regardless of (highly uncertain) seasonal mean rainfall projections. We found that current GCMs are unable to reproduce the observed rate or spatial pattern of extreme rainfall intensification, presumably linked to their inability to capture key physical processes responsible for organised convection. For example, convective parameterisations are insensitive to shear and exhibit a rather weak dependence on moisture in the free troposphere[30]. New high resolution (sub 5km) convection-permitting simulations are needed to explore how MCSs respond to enhanced Saharan warming. As the world continues to warm, we may find rapid MCS intensification signals emerging in other regions of the world where the Clausius-Clapeyron relationship (and indeed current GCM extreme rain projections) are of little value. In West Africa, the impact of recent severe flash floods provides an indication of the challenges ahead for urban planners. For example a downpour of 263 mm over several hours forced 150,000 residents of Ouagadougou (Burkina Faso) to leave their homes in 2009. Further intensification of MCSs will reduce flood return times, and increase the risk of disease

outbreaks due to poor sanitation systems. Reliable information on the changing hydroclimate therefore urgently needs to be incorporated into plans for West Africa's rapidly expanding cities.

References

1 Allen, M. R. & Ingram, W. J. Constraints on future changes in climate and the hydrologic cycle. *Nature* **419**, 224-232 (2002).

2 Westra, S. *et al.* Future changes to the intensity and frequency of short-duration extreme rainfall. *Reviews of Geophysics* **52**, 522-555, doi:10.1002/2014rg000464 (2014).

3 Min, S.-K., Zhang, X., Zwiers, F. W. & Hegerl, G. C. Human contribution to more-intense precipitation extremes. *Nature* **470**, 378-381, doi:10.1038/nature09763 (2011).

4 Donat, M. G., Lowry, A. L., Alexander, L. V., Ogorman, P. A. & Maher, N. More extreme precipitation in the world's dry and wet regions. *Nature Clim. Change* **6**, 508-513, doi:10.1038/nclimate2941 (2016).

5 Kundzewicz, Z. W. *et al.* Flood risk and climate change: global and regional perspectives. *Hydrological Sciences Journal* **59**, 1-28, doi:10.1080/02626667.2013.857411 (2014).

6 Kendon, E. J. *et al.* Heavier summer downpours with climate change revealed by weather forecast resolution model. *Nature Clim. Change*, doi:10.1038/nclimate2258 (2014).

7 O'Gorman, P. A. Precipitation Extremes Under Climate Change. *Current Climate Change Reports* **1**, 49-59, doi:10.1007/s40641-015-0009-3 (2015).

8 Houze, R. A. Mesoscale convective systems. *Reviews of Geophysics* **42**, doi:10.1029/2004rg000150 (2004).

9 Zipser, E. J., Liu, C., Cecil, D. J., Nesbitt, S. W. & Yorty, D. P. Where are the most intense thunderstorms on earth? *Bull. Am. Meteorol. Soc.* **87**, 1057-1071, doi:10.1175/BAMS-87-8-1057 (2006).

10 Biasutti, M., Held, I. M., Sobel, A. H. & Giannini, A. SST forcings and Sahel rainfall variability in simulations of the twentieth and twenty-first centuries. *J. Climate* **21**, 3471-3486 (2008).

11 O'Gorman, P. A. Sensitivity of tropical precipitation extremes to climate change. *Nature Geosci* **5**, 697-700, doi:10.1038/ngeo1568 (2012).

12 Singleton, A. & Toumi, R. Super-Clausius–Clapeyron scaling of rainfall in a model squall line. *Q. J. R. Meteorol. Soc.* **139**, 334-339, doi:10.1002/qj.1919 (2013).

13 Berg, P., Moseley, C. & Haerter, J. O. Strong increase in convective precipitation in response to higher temperatures. *Nature Geosci*, doi:10.1038/ngeo1731 (2013).

14 Muller, C. Impact of Convective Organization on the Response of Tropical Precipitation Extremes to Warming. *J. Climate* **26**, 5028-5043, doi:10.1175/JCLI-D-12-00655.1 (2013).

15 Mathon, V., Laurent, H. & Lebel, T. Mesoscale convective system rainfall in the Sahel. *J. Appl. Meteorol.* **41**, 1081-1092 (2002).

16 Futyan, J. M. & Genio, A. D. D. Deep Convective System Evolution over Africa and the Tropical Atlantic. *J. Climate* **20**, 5041-5060, doi:10.1175/jcli4297.1 (2007).

17 Panthou, G., Vischel, T. & Lebel, T. Recent trends in the regime of extreme rainfall in the Central Sahel. *Int. J. Climatol.*, doi:10.1002/joc.3984 (2014).

18 Giannini, A., Saravanan, R. & Chang, P. Oceanic forcing of Sahel rainfall on interannual to interdecadal time scales. *Science* **302**, 1027-1030 (2003).

19 Dong, B. & Sutton, R. Dominant role of greenhouse-gas forcing in the recovery of Sahel rainfall. *Nature Clim. Change* **5**, 757-760, doi:10.1038/nclimate2664 (2015).

20 Evan, A. T., Flamant, C., Gaetani, M. & Guichard, F. The past, present and future of African dust. *Nature* **531**, 493-495, doi:10.1038/nature17149 (2016).

21 Dardel, C. *et al.* Re-greening Sahel: 30 years of remote sensing data and field observations (Mali, Niger). *Remote Sens. Environ.* **140**, 350-364, doi:http://dx.doi.org/10.1016/j.rse.2013.09.011 (2014).

22 Cook, K. H. & Vizy, E. K. Detection and Analysis of an Amplified Warming of the Sahara Desert. *J. Climate* **28**, 6560-6580, doi:10.1175/jcli-d-14-00230.1 (2015).
23 Rotunno, R., Klemp, J. B. & Weisman, M. L. A Theory for Strong, Long-Lived Squall Lines. *J. Atmos. Sci.* **45**, 463-485 (1988).
24 Alfaro, D. A. Low-Tropospheric Shear in the Structure of Squall Lines: Impacts on Latent Heating under Layer-Lifting Ascent. *J. Atmos. Sci.* **74**, 229-248, doi:10.1175/jas-d-16-0168.1 (2017).
25 Barnes, G. M. & Sieckman, K. The environment of fast- and slow-moving tropical mesoscale convective cloud lines. *Mon. Weather Rev.*, 1782-1794 (1984).
26 Roca, R., Lafore, J.-P., Piriou, C. & Redelsperger, J.-L. Extratropical Dry-Air Intrusions into the West African Monsoon Midtroposphere: An Important Factor for the Convective Activity over the Sahel. *J. Atmos. Sci.* **62**, 390-407, doi:10.1175/jas-3366.1 (2005).
27 Skinner, C. B. & Diffenbaugh, N. S. Projected changes in African easterly wave intensity and track in response to greenhouse forcing. *Proceedings of the National Academy of Sciences* **111**, 6882-6887, doi:10.1073/pnas.1319597111 (2014).
28 Seidel, D. J. & Randel, W. J. Variability and trends in the global tropopause estimated from radiosonde data. *Journal of Geophysical Research: Atmospheres* **111**, doi:10.1029/2006jd007363 (2006).
29 Parker, D. J., Thorncroft, C. D., Burton, R. R. & Diongue-Niang, A. Analysis of the African easterly jet, using aircraft observations from the JET2000 experiment. *Q. J. R. Meteorol. Soc.* **131**, 1461-1482 (2005).
30 Del Genio, A. D. Representing the Sensitivity of Convective Cloud Systems to Tropospheric Humidity in General Circulation Models. *Surveys in Geophysics* **33**, 637-656, doi:10.1007/s10712-011-9148-9 (2012).

Acknowledgements. The research leading to these results received funding from the NERC/DFID Future Climate For Africa programme under the AMMA-2050 project, grant numbers NE/M020428/1, NE/M019969/1, NE/M019950/1, NE/M020126/1 and NE/M019934/1. DP is supported by a Royal Society Wolfson Research Merit Award. We thank Ken Knapp, John Marsham and Dominic Kniveton for their helpful comments, John Griffin for assistance in preparing the figures, along with the providers of key datasets used here; Eumetsat, NOAA, NASA, ECMWF, the meteorological services of Mali, Burkina Faso, Niger and Benin, and the World Climate Research Programme's Working Group on Coupled Modelling, and the centres who provided modelling data.

Author Contributions: This study was conceived by CT and TV. CT, DB, FG, DP, TV and SJ designed the research, CT, DB, FG, PH, CK and GP analysed the data, and OB provided expertise on the GPS analysis. CT wrote the manuscript, which all authors commented on.

Author Information: The authors declare no competing financial interests.

Figure Captions and Table

Figure 1 Trends in MCS and rainfall characteristics. (a) Annual rainfall, and (b) contribution of extreme events to annual rainfall from a daily rain gauge network (red lines: 5-year running means). (c,d) Regional MCS frequency at 1800 UTC at different temperature thresholds, derived from MFG

(+), MSG (O) and Gridsat (solid line) data. Dotted lines denote trends. (e) Significant trends ($p<0.05$) in MCS cloud cover at 1800 UTC (using a temperature threshold of -70°C). Trends are expressed as the percentage change per decade, relative to the 35 year mean (contours). The red and purple rectangles denote the domains used in (a,b) and (c,d) respectively.

Figure 2 Temperature trends (JJAS) in observations and models. Trends (°C decade^{-1}) are derived from (a) synoptic stations, (b) ERA-Interim reanalysis, (c) lower tropospheric temperature derived from microwave sounding data, and (d) CMIP5 ensemble mean for historical runs. (e) Meridional temperature gradient (20°N minus 10°N, average over 15°W-15°E) from CMIP5 historical (red), RCP4.5 (green) and RCP8.5 (purple) ensembles (relative to 1961-1990; shading denotes the ensemble standard deviation). Temperatures are at 2m height, apart from (c) which samples the lower troposphere. Trends are computed for the period 1982-2015, apart from (d), which is 1976-2005. Significant positive and negative trends ($P<0.05$) are denoted by solid black circles (a), or lie within blue contours (b,c).

Figure 3 Evolution of observed PW from GPS stations. (a) Composite mean PW (mm) associated with the passage (at 0 hours) of 496 Sahelian MCSs. Small (large) circles denote times when PW is significantly correlated with MCS intensity for $P<0.05$ ($P<0.01$). (b) Evolution of PW anomalies sampled from events in the lower (blue) and upper (red) quartiles of MCS temperature. Circles denote times when the two time series differ significantly ($P<0.05$).

Table 1 Linear correlation statistics for 24-hour mean MCS frequency at different temperature thresholds. Global land mean temperatures (shown in Extended Figure 1c) are computed from JJAS averages.

Temperature threshold, °C	Correlation coefficient (p-value)		
	Linear trend	Sahel rain	Global temperature
-40	0.41 (0.007)	0.88 (<0.00001)	0.37 (0.0162)
-60	0.77 (<0.00001)	0.83 (0.00015)	0.77 (<0.00001)
-70	0.87 (<0.00001)	0.65 (0.00002)	0.82 (<0.00001)
-75	0.88 (<0.00001)	0.56 (0.00036)	0.80 (<0.00001)

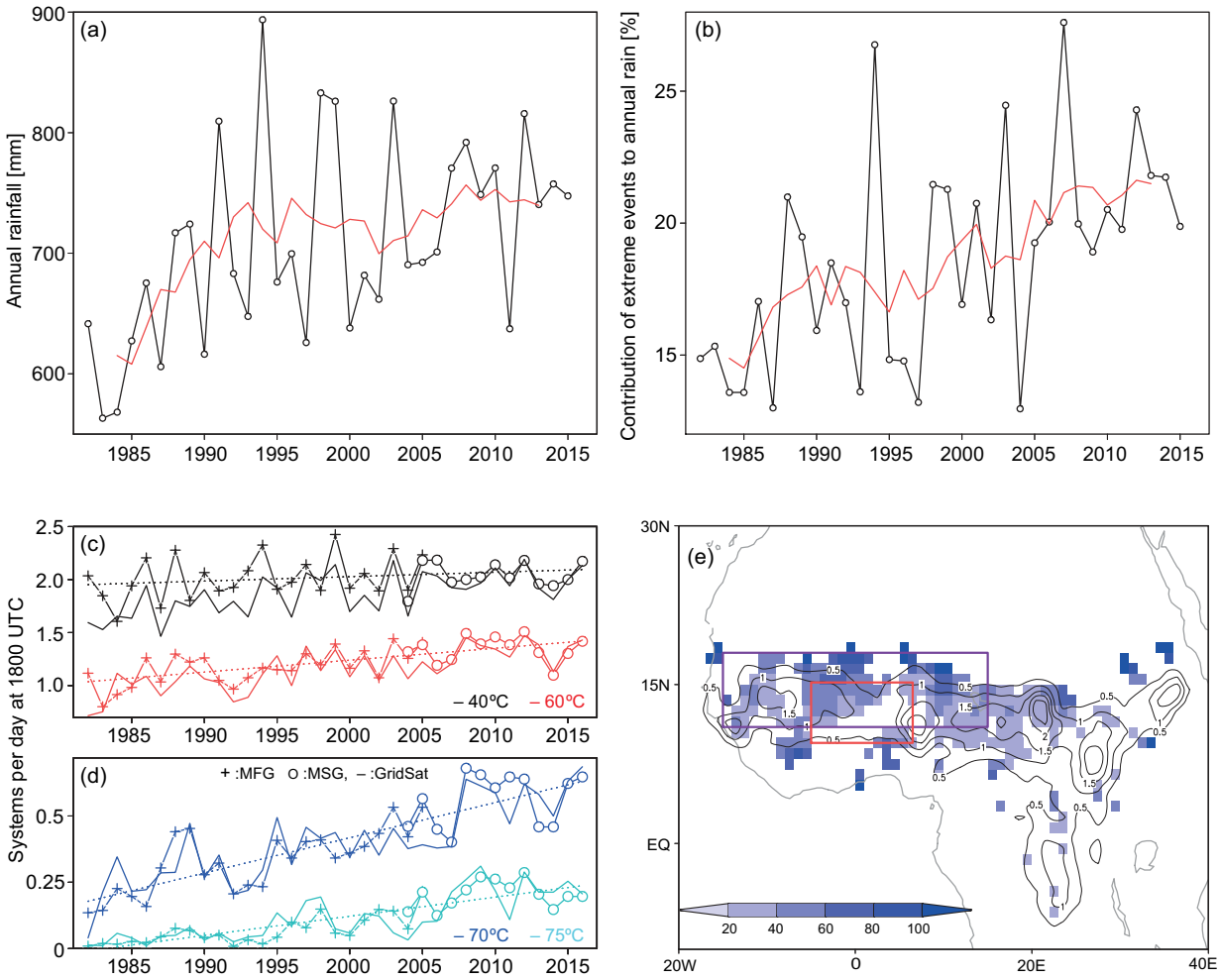
(a)
Annual rainfall [mm]
900
800
700
600
1985
1990
1995
2000
2005
2010
2015
(b)
Contribution of extreme events to annual rain [%]
25
20
15
(c)
Systems per day at 1800 UTC
2.5
2.0
1.5
1.0
– 40°C
– 60°C
(d)
+ :MFG O :MSG, – :GridSat
0.5
0.25
0
– 70°C
– 75°C
(e)
30N
15N
EQ
20W
0
20E
40E
20
40
60
80
100

Figure 1

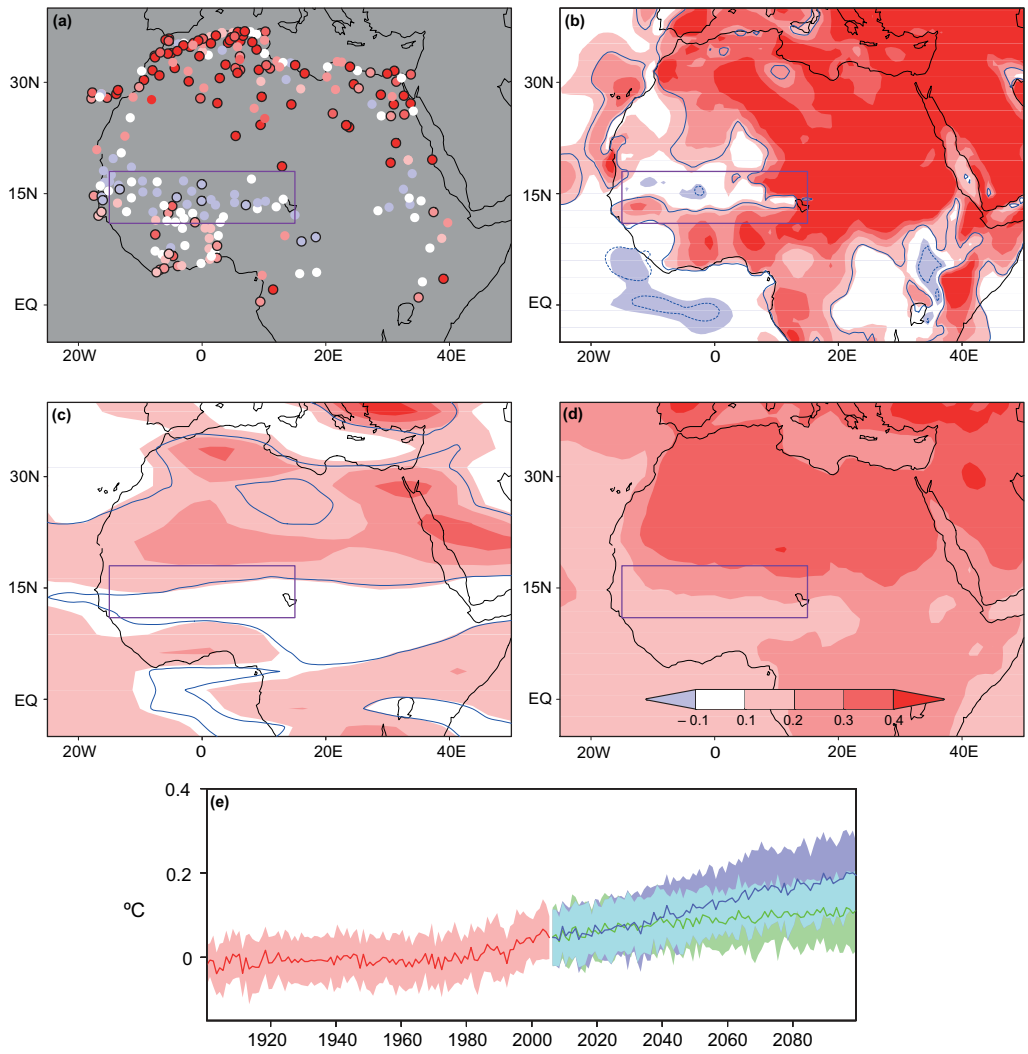
(a)
(b)
(c)
(d)
(e)
30N
15N
EQ
20W
0
20E
40E
− 0.1
0.1
0.2
0.3
0.4
°C
0.4
0.2
0
1920
1940
1960
1980
2000
2020
2040
2060
2080

Figure 2

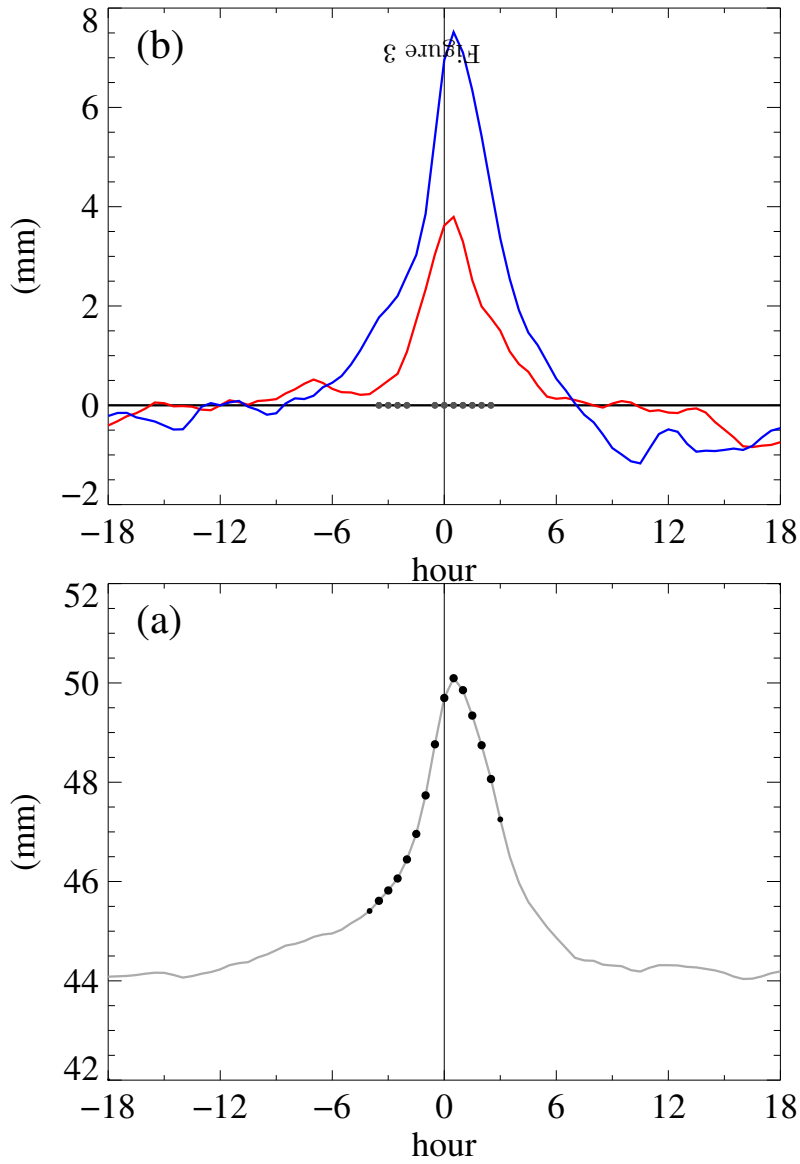
(b)
Figure 3
8
6
4
2
0
−2
(mm)
−18
−12
−6
0
6
12
18
hour
(a)
52
50
48
46
44
42
(mm)
−18
−12
−6
0
6
12
18
hour

Methods

Cloud-top temperature data

The principal dataset used in this study is cloud-top temperature, observed from the series of geostationary Meteosat satellites, which we use to quantify the evolution of MCS characteristics. As the satellites are located at 0°E, 0°N, these data provide excellent coverage of tropical Africa. Archived data (downloaded from Eumetsat, http://www.eumetsat.int) are available from 1982 to the present. We use measurements from 9 satellites in the series, from Meteosat-2 (1982) to Meteosat-10 (2016). Meteosat First Generation (MFG; ending in July 2006) satellites carried the Meteosat Visible and Infrared Imager, providing Thermal Infrared data (10.5-12.5μm) every 30 minutes at a resolution ~ 4.5km at the equator. From 2004 onwards this was superseded by the Spinning Enhanced Visible and Infrared Imager on Meteosat Second Generation (MSG) platforms. This provides higher spatial (~3km) and temporal (15 minutes) resolution and additional channels - here we use MSG channel 9 (centred at 10.8μm). We used the coefficients provided by Eumetsat to convert the data from counts to brightness temperature (http://www.eumetsat.int/website/home/Data/Products/Calibration/index.html). Up to May 2000, a vicarious calibration technique was adopted using a sea surface target. Top of atmosphere radiance was estimated using data from the National Centers for Environmental Prediction analysis. Since then, the Meteosat sensors have benefited from an onboard black-body calibration mechanism. To minimise the impact of the change in pixel size from MFG to MSG, we degraded the images to an approximately common resolution of 9km (2x2 MFG pixels, 3x3 MSG pixels), and only used half-hourly MSG data.

For a given temperature threshold, we define MCSs in each image from contiguous cold cloud systems which exceed an areal threshold of 25,000 km^2. We chose this areal threshold based on comparison of cold cloud structures with daily rain gauge measurements (see below). Four temperature thresholds are used, -40, -60, -70 and -75°C. We define a geographical domain spanning the Western and Central Sahel (15°W-15°E, 11-18°N, plotted in Figure 1e) over which we computed MCS properties for every available half-hourly image for the monsoon months of June to September. Each MCS centred within the domain was counted, and Figures 1c and d present these data (for 1800 UTC) as the sum of MCSs divided by the number of images available in that season. Trends in MCS frequency at other times of day are shown in Extended Figure 3, and correlations of the 35-year time series in Table 1 are computed using average MCS frequencies over all 48 images within a day. We found that on average, the daily minimum in the minimum temperature for each MCS at a threshold

of -40°C occurred at 1700 UTC, denoting the end of the vertical development phase[16] and the onset of the mature phase, marked by horizontal growth. The likelihood of observing intense rainfall rates from spaceborne precipitation radar data (see below) was maximised during the period 1800-2100 UTC, associated with mature MCSs. When assessing spatial variations in trends (Figures 1e), for each image we computed the fractional coverage of pixels within an MCS at 1° spatial resolution. Throughout, trends in MCS frequency are expressed as a percentage relative to the mean.

We explored the sensitivity of MCS properties to different temperature thresholds using independent observations. This was to verify that lower temperature thresholds are on average representative of more intense MCSs. The westward propagation speed was computed for every MCS in consecutive half-hourly images by identifying the length scale at which the maximum spatial correlation of brightness temperatures occurred. This revealed a clear sensitivity of propagation speed, with mean values of 12.0, 14.4, 16.6 and 18.3 ms^{-1} for MCS temperature thresholds of -40, -60, -70, and -75°C respectively. We also computed the likelihood of MCS passage over an individual raingauge on a day which received intense rainfall, and how this likelihood varied with areal threshold and cloud top temperature (Extended Figure 2a,b). Using 19 Sahelian stations at latitudes between 13.0 and 15.3°N, the minimum cloud-top temperature and maximum contiguous cloud area affecting pixels within 7.5 km of the gauge were recorded for each day with rain exceeding 10mm. We examined those data where rain exceeded an intense rainfall threshold, based on the average of individual station thresholds (see below), which for this limited range of latitudes gave 38mm. Whilst a small fraction of these cases (12%) registered no local cold cloud (-40°C or less) over 24 hours, overall the likelihood of intense rain coinciding with an MCS at a temperature threshold of -40°C and areal threshold of 25,000km^2, was 85.5% (rising to 96% if no cold-cloud cases were excluded; Extended Figure 2a). Considering only cases where this areal threshold was satisfied, Extended Figure 2b illustrates the expected strong sensitivity of daily rainfall to minimum pixel temperature. We found that 88% of all extreme events are associated with minimum temperatures of -70°C or lower, and the coldest 20% of cloud-top temperatures account for nearly one third of the extreme measurements.

Finally, we overlaid the MCS dataset (with a threshold of -40°C) in space and time, with precipitation radar data from 1640 overpasses from the Tropical Rainfall Measurement Mission (TRMM) over the period 2004-2013. Radar-based estimates of surface rainfall rate and the type of rain (convective or stratiform) are provided within the TRMM2A25 product (available from http://disc.sci.gsfc.nasa.gov/precipitation). Extended Figure 2c clearly illustrates how the probability of extreme rainfall rate (defined here as the 98th percentile of all TRMM observations, equivalent to

30 mm hour^{-1}) within an MCS rises with decreasing MCS temperature. We found that 38% of extreme events are associated with the coldest 20% of MCSs. We also examined the rainfall type for all TRMM pixels with non-zero rain within each MCS. We found that the fraction of rainy pixels which were convective rose from 20% to 30% as the mean MCS temperature decreased from -40°C to -70°C.

The Meteosat series was designed for the operational meteorological community rather than long-term monitoring. To address the needs of climate research, recent efforts have been made to homogenise these data, alongside other geostationary series, resulting in the global GridSat climate data record[31]. This dataset built on the work of the International Satellite Cloud Climatology Project (ISCCP), which provided an absolute calibration of geostationary measurements through use of Advanced Very High Resolution Radiometer data on board polar-orbiting satellites. The GridSat product benefits from a second inter-calibration with observations from the High-Resolution Infrared Radiation Sounder. This additional step allowed for the detection and correction of biases in the ISCCP product[31,32]. The estimated calibration uncertainty in this product is less than 0.1 °C per decade. The data (available at www.ncdc.noaa.gov/gridsat) are corrected for view angle and parallax and stored on a 0.07° grid every 3 hours. We used GridSat data spanning the period January 1982 to September 2016.

We focus in this study on the frequency of MCSs at different temperature thresholds, a measure which is rather insensitive to biases and drifts in brightness temperature when using the uncorrected Eumetsat dataset. This important aspect is illustrated in Figures 1c and d, which show a high degree of consistency in MCS frequency between Meteosat-7 (from the MFG series) and Meteosat-8 (the first MSG satellite) during the MFG/MSG overlap period of 2004-5. Crucially, the trends in MCS frequency based on the Eumetsat data are reproduced by the GridSat record. Moreover, time series of mean MCS temperature (at -40°C) exhibit a clear downward trend over the 35 years (Extended Figure 4), with no evident breaks associated with changes in satellite. Final evidence to support our use of satellite data in trend detection is provided in Figure 1e and Extended Figure 5. These show positive trends in MCS frequency only in specific regions in Africa. A series of sensor drifts across instruments and, in the case of GridSat, cross-calibration errors, would contribute to positive trends everywhere that MCSs occur.

Rain gauge data

We used daily rainfall data from 42 sites located between 9.6 and 15.3 °N, 4.8°W and 6.1 °E for the period 1950 to 2015 to analyse changes in the contribution of extreme daily rain to seasonal totals in Figure 1 (44 sites in Extended Figure 1). We repeated the methodology used in a previous study[17],

where extreme daily rain is defined as that which exceeds a given threshold (constant over the period, but varying from one gauge to another). This threshold was defined using Extreme Value Theory and corresponds to the expected value which is exceeded twice a year. To quantify JJAS-mean rainfall across the larger domain (15°W-15°E, 11-18°N), we used the CRU 3.23 monthly gridded rainfall dataset (available from https://crudata.uea.ac.uk/cru/data/hrg/cru_ts_3.23/). Interannual rainfall in this dataset is highly correlated with the frequency of MCSs at a threshold of -40°C for the period 1982-2014 (Table 1).

Precipitable water data

The Global Positioning System (GPS) precipitable water (PW) data used in this study come from 4 stations in Mali, Burkina Faso and Niger, operated between 2005 and 2011, and processed with GAMIT v10.32 scientific software in high precision mode[33]. The GPS PW is an estimate of the total column water vapour. However, due to the geometry of the measurement, and since water vapour is mostly concentrated in the lower troposphere, GPS PW reflects variations of water vapour within a horizontal radius of 20-25 km around the site, and the lowest 4-5 km vertically. For Figure 3 we computed mean PW every 30 minutes relative to MCS time of arrival at the GPS station (according to Meteosat data). To avoid oversampling, we discarded events when they were separated by less than 6 hours from the previous MCS. For the correlations between PW and MCS intensity, we used the minimum brightness temperature recorded locally. A total of 496 events was detected over the four sites between 1500 and 2100 UTC, and these events were combined to build the composite presented in Figure 3. The moistening (drying) trend preceding (following) the passage of an MCS in Figure 3 is qualitatively consistent with measurements in other tropical regions[34].

Analysis of atmospheric variables

In situ observational data networks are both sparse and temporally heterogeneous in many parts of North Africa, particularly the Sahara. We therefore examined historic temperature trends with multiple datasets. Trends in JJAS temperatures at 2m in Figure 2 and Extended Figure 6 are based on in situ observations (SYNOP data downloaded from http://database.amma-international.org, and data compilations from Berkeley Earth[35], GHCN v3.3.0 [36], CRUTEM4.3[37] available from http://berkeleyearth.org/data/ , http://www.metoffice.gov.uk/hadobs/crutem4/) and atmospheric reanalyses (ERA-Interim[38] and MERRA-2, available from http://www.ecmwf.int/en/research/climate-reanalysis/era-interim and https://gmao.gsfc.nasa.gov/reanalysis/MERRA-2/). We also include trends computed from Microwave Sounding Unit (MSU) lower tropospheric temperature retrievals

from multiple satellites[39] (version 5.6 downloaded from ghrc.nsstc.nasa.gov/home). This retrieval samples temperatures up to about 8 km, but is strongly weighted towards the lowest 3-4 km. As shown previously[22], the detailed patterns of warming in North Africa are not always consistent across different reanalyses, or indeed in gridded screen level temperature datasets. We therefore interpret detailed structure in individual reanalysis trends with caution. For example, there is a pronounced low level warming across the Sahelian zone of Chad (15-25°E, 10-15°N) in ERA-Interim which is not found in the other datasets.

We performed correlation analysis between atmospheric properties and MCS intensity (as measured by mean temperature of the MCS) on the event time scale, using reanalysis data from ERA-Interim. We identified 99 MCSs which appeared in the Niamey region of Niger (2-3°E, 13-14°N) between the hours of 1500 and 2100 UTC over the period 2004-16. We chose this location as the local radiosonde station regularly provides data for assimilation within ERA-Interim. Indeed we found the region between Niamey and Ouagadougou, Burkina Faso (1.5°W, 12.4°N) provided the best agreement of any Sahelian location in terms of time series of temperature depicted in the ERA-Interim and MERRA-2 reanalyses. We computed correlations between observed MCS temperature (at time of appearance) with local temperature, wind and humidity variables from the preceding 1200 UTC reanalysis. In Extended Figure 7 we include only those variables which have significant correlations (at the 95% level); precipitable water, and specific humidity and vorticity at 925 hPa failed this test. We found that more intense MCSs are positively correlated, at both 925 and 700 hPa, with increased temperature, weaker southerly wind, and reduced relative humidity. In addition, more intense MCSs are, on average, preceded by stronger low level westerlies and mid-level (600 hPa) easterlies. In terms of zonal wind, the correlations are stronger considering the difference between these two levels than individually (Extended Figure 7e).

To link our results to long-term, large-scale trends in the monsoon, we also computed correlations between atmospheric variables (from ERA-Interim) and observed MCS intensity using annual time series. For the atmospheric variables we computed zonal means between 15°W and 15°E on all available pressure levels, sampled daily at 1200 UTC throughout JJAS. In the case of the meridional wind variance, an indicator of synoptic variability, we first calculated seasonal mean variance for each grid point using the anomaly from a 5-day running mean. For MCS intensity we used the annual time series of temperatures shown in Extended Figure 4. Extended Figure 8 presents the correlations as a set of meridional cross-sections through the WAM. Because the observed MCS temperature

time series used in this analysis is rather linear (correlation coefficient of -0.81 when averaged across different times of day), the spatial structure of the correlations with MCS intensity closely resembles that of the trend in the different variables (shown for temperature and wind components in Extended Figure 8g-i). The trend towards more intense MCSs is correlated with rising temperatures throughout the Saharan PBL (up to around 600 hPa north of 20°N), and its southerly extension, the SAL, which overlies the shallower Sahelian PBL. We interpret the correlation patterns of the dynamical variables in terms of this warming; the thermal wind strengthening low level westerlies and mid-level easterlies (Extended Figure 8b,h) to the south of the enhanced Saharan Heat Low; increased southerly winds driven by the enhanced meridional temperature gradient (and "downgliding" along isentropic surfaces, which tilt equatorward with height; Extended Figure 8 c,i); increased synoptic variability below 700 hPa in the Northern Sahel and Southern Sahara, consistent with increased baroclinic instability. Note that we also considered potential impacts of sub-seasonal sampling on our interannual correlations. Specifically, we compared trends in midday atmospheric variables sampling all days, with trends computed using only data from days and locations where MCSs were detected either the following, or previous afternoon or evening. Trends in both pre- and post-event low level temperatures in the Sahel were slightly negative, indicating that intensifying MCSs are not the primary cause of long-term Sahelian cooling. The mean cooling is more likely related to the increasing frequency of moderate MCSs, rainfall and cloudiness.

The long-term observational upper air record in the Sahel is very sparse, both geographically, and in terms of pressure levels for which key variables are reported. We examined monthly-mean series from IGRA[40] (ftp://ftp.ncdc.noaa.gov/pub/data/igra/v2beta/), RATPAC-B[41] (ftp://ftp.ncdc.noaa.gov/pub/data/ratpac), and Yale[42], all based on sounding data but using different correction and adjustment procedures, and from the radiosonde archive maintained by the University of Wyoming (http://weather.uwyo.edu/upperair/sounding.html), as well as monthly-mean gridded products HadAT[43] (http://www.metoffice.gov.uk/hadobs/hadat/) and RAOBCORE and RICH[44] (ftp://srvx7.img.univie.ac.at/). We were able to confirm from these datasets the existence of a trend in both warming of the SAL (at 700 hPa) relative to the underlying PBL (at 850 hPa), and increased easterlies at 700 hPa.

To shed light on the role of anthropogenic emissions of greenhouse gases and aerosols, we include diagnostics from the CMIP-5 GCM ensemble[45] (http://cmip-pcmdi.llnl.gov/cmip5/data_portal.html). We used 37 models run under both the historical and historicalNat scenarios to create Figure 2d and Extended Figure 6d. Trends were first computed on each model's native grid and then interpolated to

a common resolution. The time series in Figure 2e were based on this same set of models for the historical (1850-2005) and future (2006-2100) scenarios (both RCP4.5 and RCP8.5). The ensemble of historical simulations were also used to assess trends in daily rainfall extremes over the period 1976-2005. For each model and grid cell we computed the 90th centile daily rainfall rate from the months JJAS over the 30 years, and counted the threshold exceedance per year. We found the ensemble mean trend in the study area was very small compared to our observations, an increase of the order of 1% over 30 years.

Data Availability

The daily station rain gauge data are subject to third-party restrictions and are not freely available. All the remaining data used in this study can be accessed free-of-charge from the repositories listed above.

References

31 Knapp, K. R. *et al.* Globally Gridded Satellite Observations for Climate Studies. *Bull. Am. Meteorol. Soc.* **92**, 893-907, doi:10.1175/2011bams3039.1 (2011).

32 Knapp, K. R. Calibration Assessment of ISCCP Geostationary Infrared Observations Using HIRS. *J. Atmos. Oceanic Technol.* **25**, 183-195, doi:10.1175/2007jtecha910.1 (2008).

33 Bock, O. *et al.* West African Monsoon observed with ground-based GPS receivers during African Monsoon Multidisciplinary Analysis (AMMA). *Journal of Geophysical Research: Atmospheres* **113**, doi:10.1029/2008jd010327 (2008).

34 Holloway, C. E. & Neelin, J. D. Temporal Relations of Column Water Vapor and Tropical Precipitation. *J. Atmos. Sci.* **67**, 1091-1105, doi:10.1175/2009jas3284.1 (2010).

35 Rohde, R. *et al.* A New Estimate of the Average Earth Surface Land Temperature Spanning 1753 to 2011. *Geoinfor Geostat: An Overview*, doi:10.4172/2327-4581.1000101 (2013).

36 Lawrimore, J. H. *et al.* An overview of the Global Historical Climatology Network monthly mean temperature data set, version 3. *Journal of Geophysical Research: Atmospheres* **116**, doi:10.1029/2011jd016187 (2011).

37 Jones, P. D. *et al.* Hemispheric and large-scale land-surface air temperature variations: An extensive revision and an update to 2010. *Journal of Geophysical Research: Atmospheres* **117**, doi:10.1029/2011jd017139 (2012).

38 Dee, D. P. *et al.* The ERA-Interim reanalysis: configuration and performance of the data assimilation system. *Q. J. R. Meteorol. Soc.* **137**, 553-597, doi:10.1002/qj.828 (2011).

39 Christy, J. R., Spencer, R. W. & Braswell, W. D. MSU Tropospheric Temperatures: Dataset Construction and Radiosonde Comparisons. *J. Atmos. Oceanic Technol.* **17**, 1153-1170, doi:10.1175/1520-0426(2000)017<1153:MTTDCA>2.0.CO;2 (2000).

40 Durre, I., Vose, R. S. & Wuertz, D. B. Overview of the Integrated Global Radiosonde Archive. *J. Climate* **19**, 53-68, doi:10.1175/JCLI3594.1 (2006).

41 Free, M. *et al.* Radiosonde Atmospheric Temperature Products for Assessing Climate (RATPAC): A new data set of large-area anomaly time series. *Journal of Geophysical Research: Atmospheres* **110**, doi:10.1029/2005jd006169 (2005).

42 Sherwood, S. C., Meyer, C. L., Allen, R. J. & Titchner, H. A. Robust Tropospheric Warming Revealed by Iteratively Homogenized Radiosonde Data. *J. Climate* **21**, 5336-5352, doi:10.1175/2008JCLI2320.1 (2008).
43 Thorne, P. W. *et al.* Revisiting radiosonde upper air temperatures from 1958 to 2002. *Journal of Geophysical Research: Atmospheres* **110**, doi:10.1029/2004jd005753 (2005).
44 Haimberger, L., Tavolato, C. & Sperka, S. Toward Elimination of the Warm Bias in Historic Radiosonde Temperature Records—Some New Results from a Comprehensive Intercomparison of Upper-Air Data. *J. Climate* **21**, 4587-4606, doi:10.1175/2008JCLI1929.1 (2008).
45 Taylor, K. E., Stouffer, R. J. & Meehl, G. A. An Overview of CMIP5 and the Experiment Design. *Bull. Am. Meteorol. Soc.* **93**, 485-498, doi:10.1175/bams-d-11-00094.1 (2011).

Extended Data Figure Captions

Extended Figure 1 Rainfall and temperature time series 1950-2015. (a) Annual mean rainfall [mm], and (b) contribution of extreme rain events to annual total [%] from the daily rainfall dataset in the Central Sahel. (c) Global land mean temperatures for JJAS from the CRU dataset. Note that data for 2015 were not included in the CRU data. Five year running means are shown as a red line.

Extended Figure 2 Comparison between observations of extreme rainfall and measures of cold cloud from MSG data. Daily rainfall (mm; data below 10 mm are excluded) recorded at 19 Sahelian gauges (2004-15) plotted against the logarithm of maximum area of contiguous cold cloud (a) and minimum brightness temperature (°C) for MCSs>25,000 km^2 (b). (c) Mean MCS temperature as a function of the maximum rainfall rate from TRMM precipitation radar based on 1640 coincident overpasses. Each point is shaded according to its normalised kernel density. The bars in the upper plots show the fractional contribution of equally-populated quintiles to the total number of extreme events (greater than 38 mm day^{-1} for a and b, greater than 30 mm $hour^{-1}$ for c).

Extended Figure 3 Diurnal cycle of MCS properties. Mean (red line) MCS frequency (left) and 90th centile cold cloud area (right) using temperature thresholds of -40°C (a, b), -60°C (c, d), -70°C (e, f), and -75°C (g, h). Also shown are the trends (black lines) in these quantities, expressed in terms of the linear regression gradient multiplied by the length of the dataset (35 years). Trends which are significant (according to a 2-tailed t-test) at the 99.5% (95%) are denoted by a circle (plus sign).

Extended Figure 4 Mean temperature of MCSs identified from GridSat data using a temperature threshold of -40°C. Temperatures (°C) are presented as JJAS averages, sampled at 4 different times of

day. Linear trends are shown as dashed lines and the value of associated correlation coefficients (r) quoted.

Extended Figure 5 Trends in MCS cloud cover at 1800 UTC. Shaded pixels denote significant trends ($p<0.05$) over the full annual cycle (a,b), March-May (c,d), Jun-Aug (e,f), Sep-Nov (g,h) and Dec-Feb (i,j) using data from 1982-2015. The left (right) hand column uses a temperature threshold of -60°C (-70 °C). Trends are expressed as the percentage change per decade, relative to the long-term mean (contours).

Extended Figure 6 Trends in 2m temperature. Trends (°C decade^{-1}) from (a) station data within the Berkeley Earth dataset, (b) MERRA-2 reanalysis, (c) GHCN station data, (d) the CMIP5 ensemble mean for the All Forcings minus Natural Forcings, and (e) the gridded station data of CRUTEM4. Trends significant at the 95% level are shown in (a) and (c) with black edges, with + signs in (e), and are enclosed with a blue contour in (b).

Extended Figure 7 Event-based correlations between pre-MCS atmospheric variables (from ERA-Interim), and observed MCS mean temperature on arrival at Niamey. All linear regressions are significant at the 99.55% according to a 2-tailed t-test, with the exception of (c), (h) and (i), which are significant at the 95% level.

Extended Figure 8 Trends and correlations with MCS intensity of zonal and annual mean variables from ERA-Interim. Correlation coefficients (shaded where significant - $P<0.05$) with (a-f) observed Sahelian MCS (-40°C threshold) mean temperature, and (g-i) year. In (a-f), contours depict mean values of (a) potential temperature (K), (b) zonal, and (c) meridional wind (ms^{-1}), (d) specific humidity (g kg^{-1}), (e) relative humidity (%), and (f) variance of meridional wind (m^{2}s^{-2}). In (g-i), the contours show the trends in (g) potential temperature (K decade^{-1}), (h) zonal, and (i) meridional wind (ms^{-1} decade^{-1}). Dotted lines depict the latitudinal limits of the Sahel. Note that negative correlations with MCS temperature (i.e. positive correlations with intensity; a-f), and positive correlations with time (g-i) are shaded red for ease of comparison.

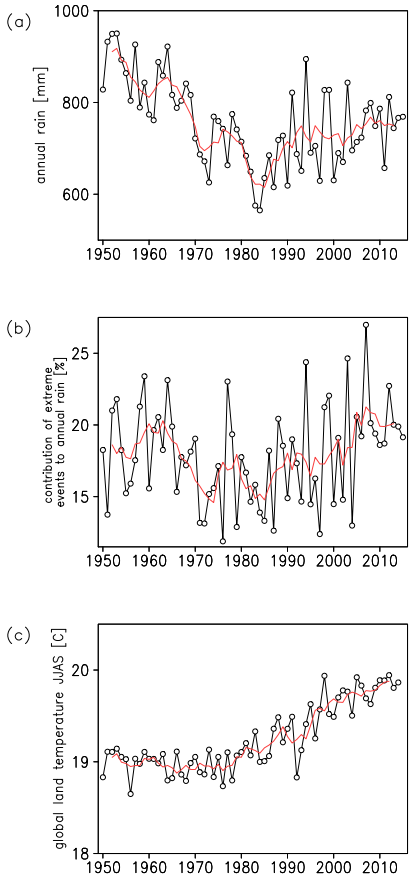

Extended Figure 1

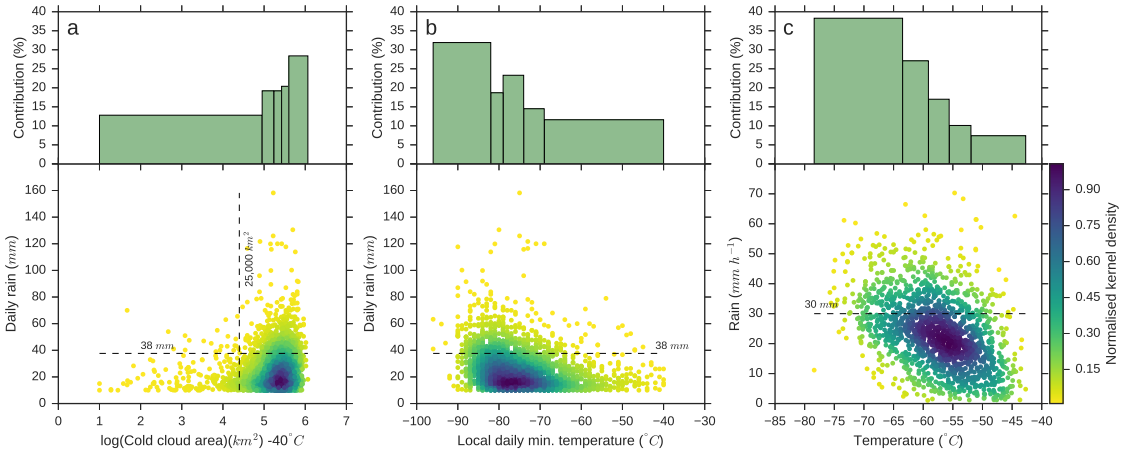

Extended Figure 2

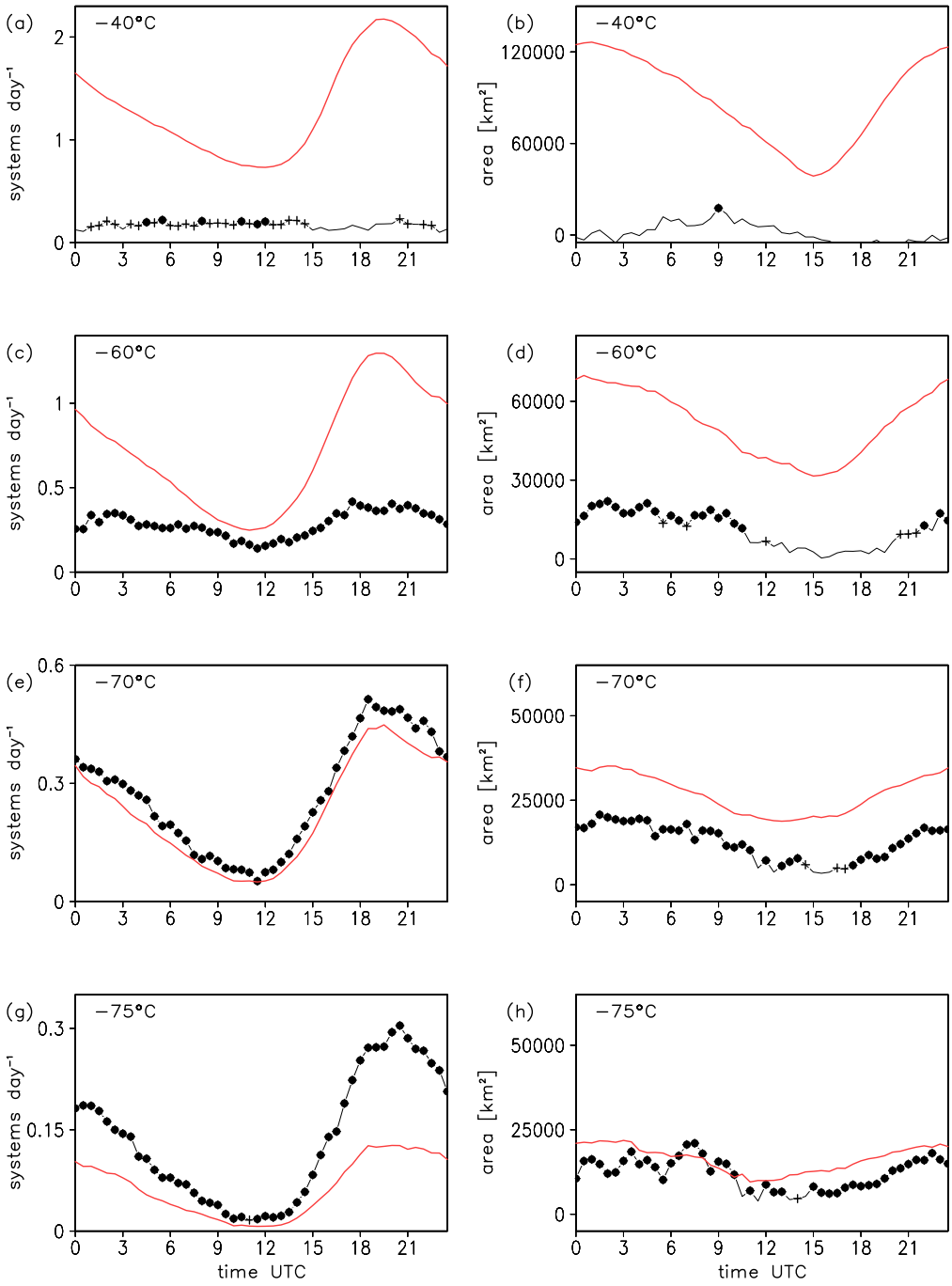

Extended Figure 3

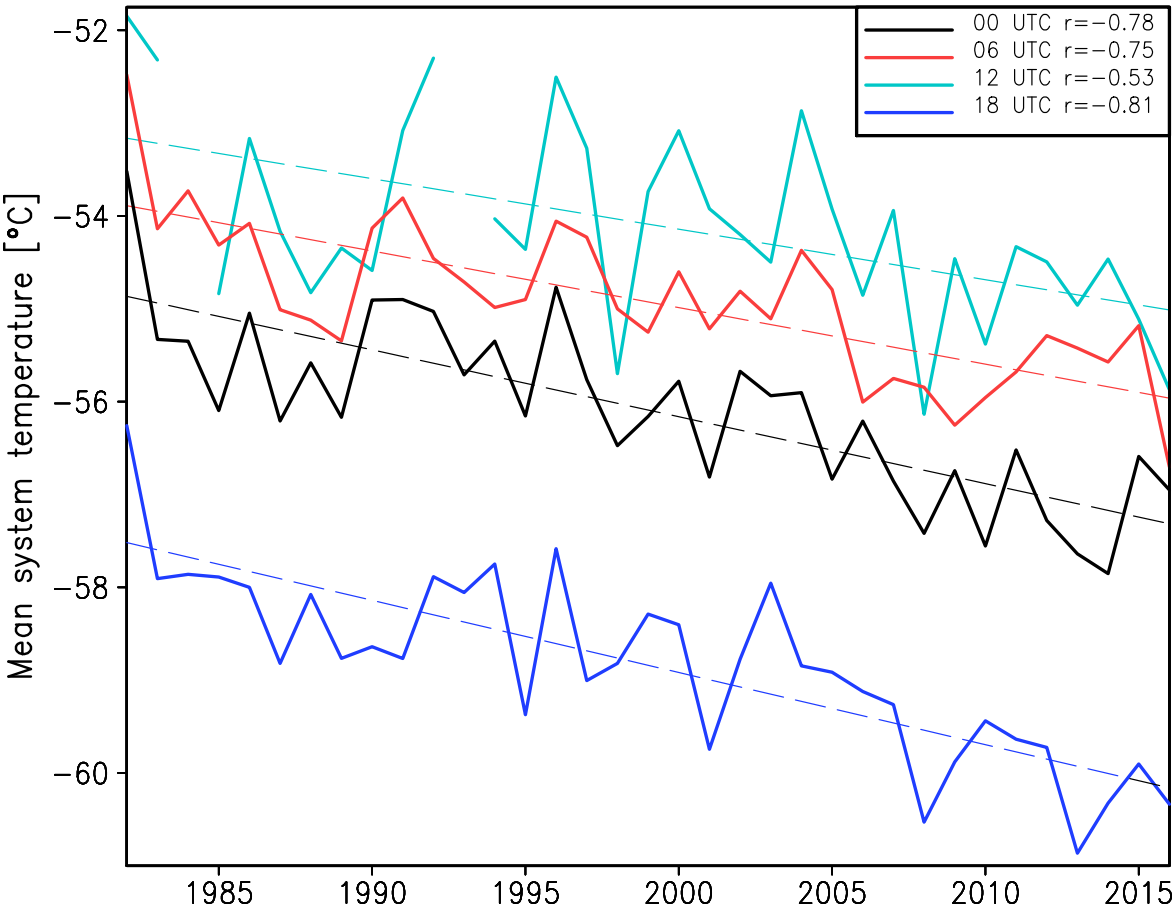

Extended Figure 4

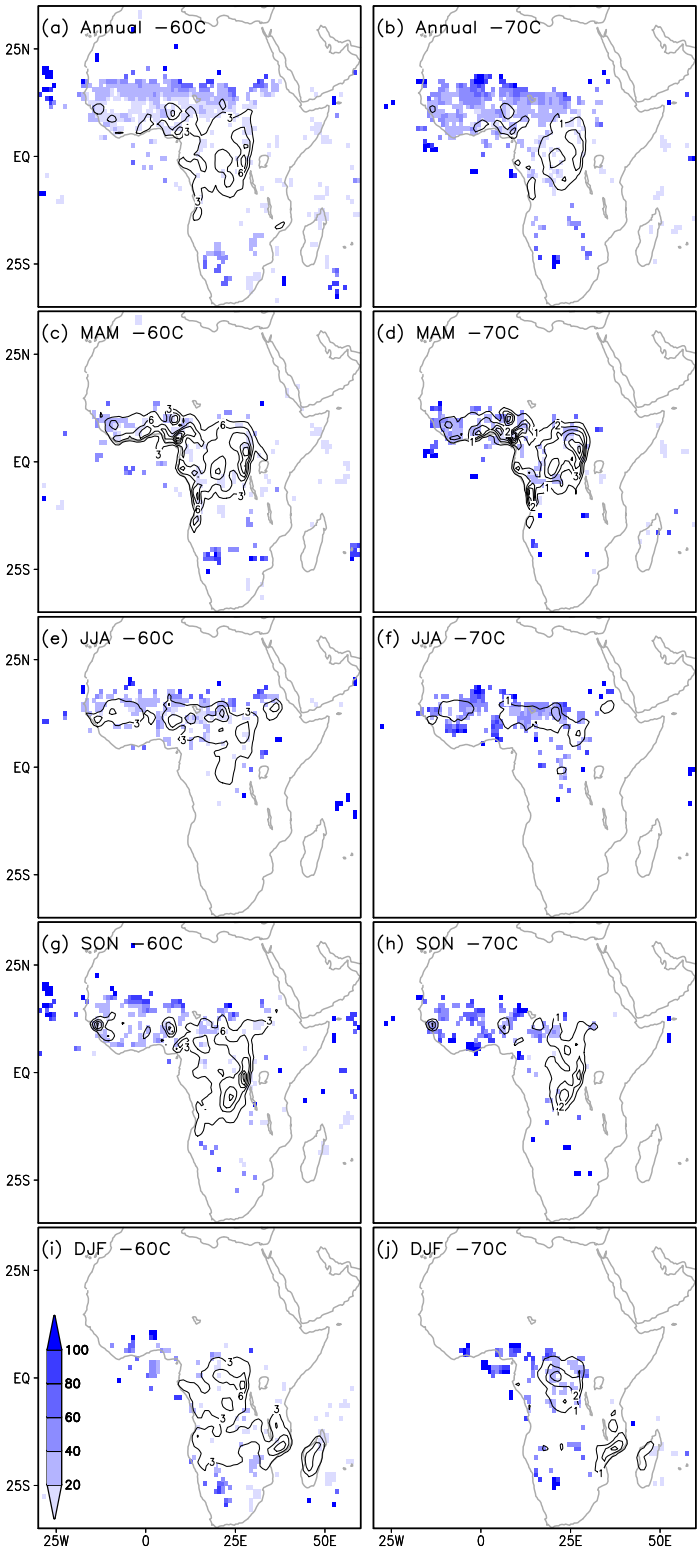

Extended Figure 5

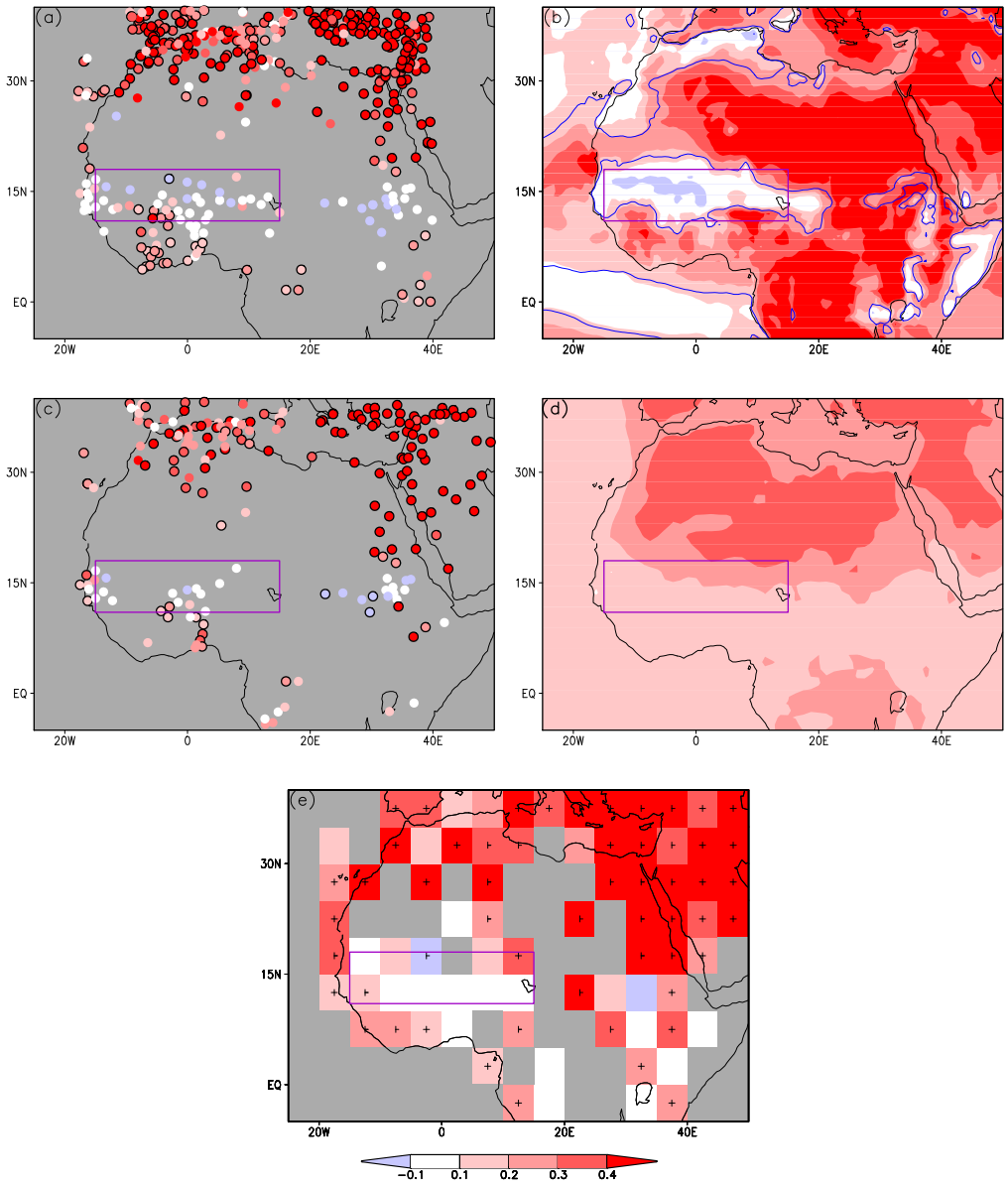

Extended Figure 6

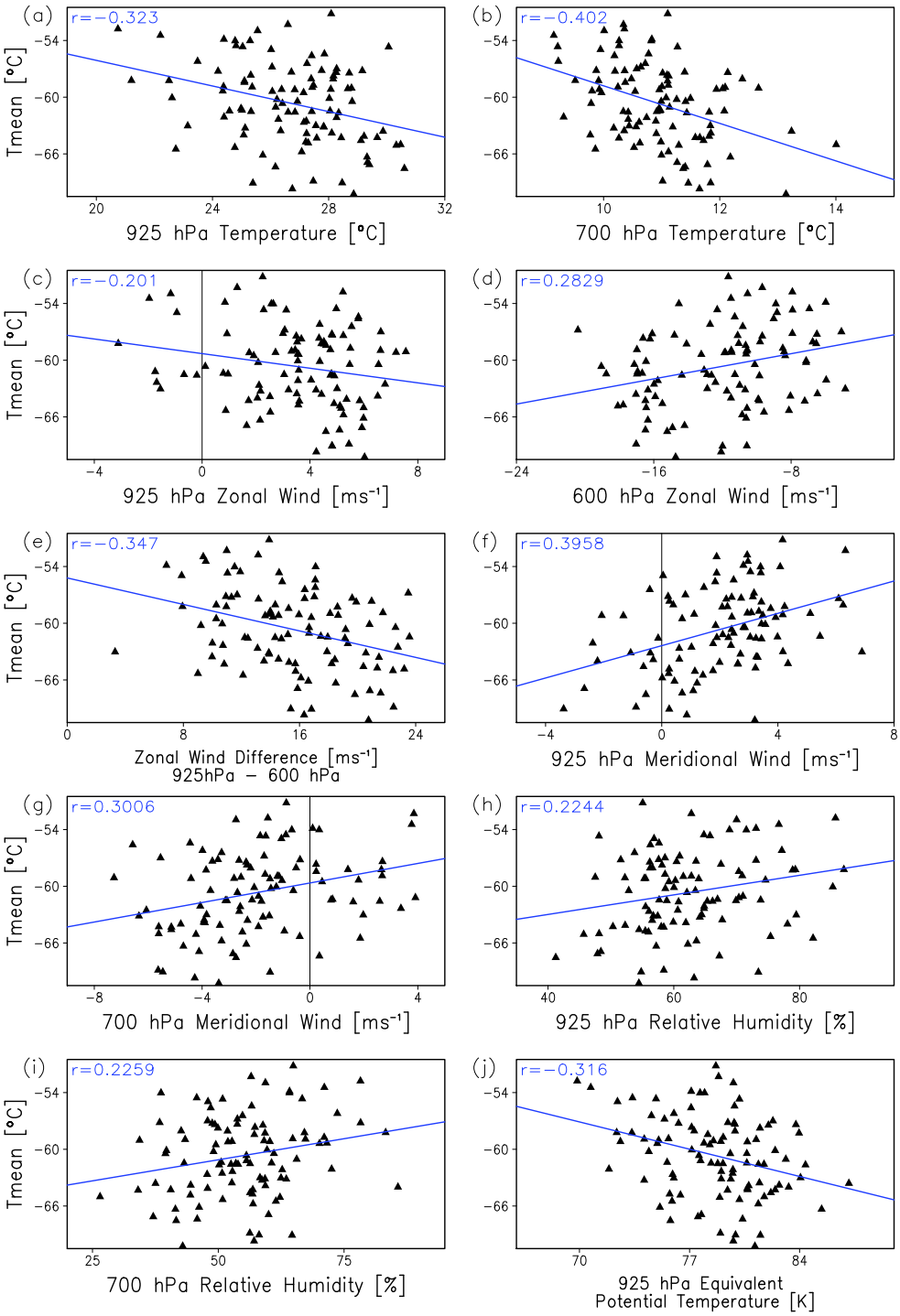

Extended Figure 7

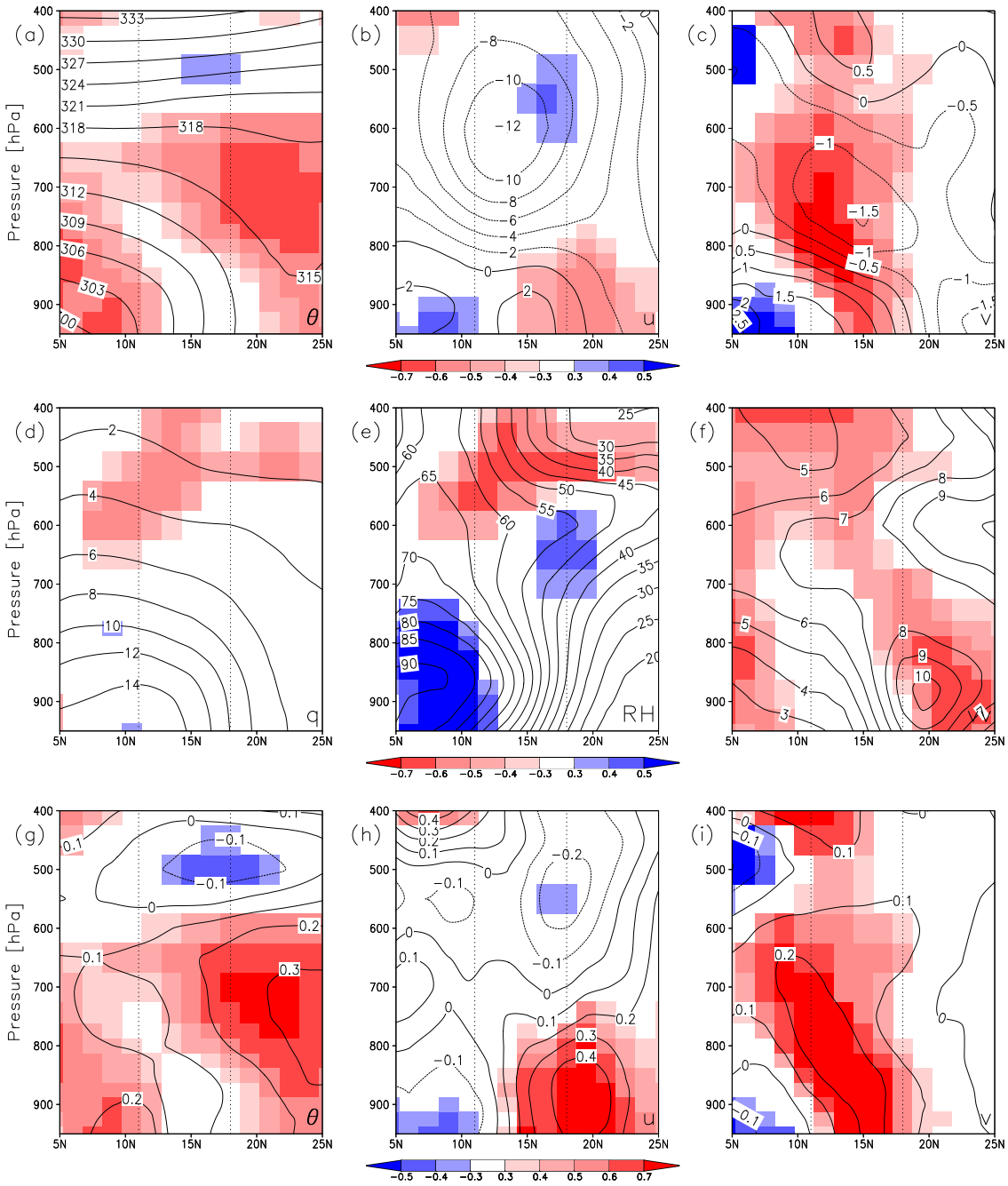

Extended Figure 8